

1 Is the Aftershock Zone Area a Good Proxy for the
2 Mainshock Rupture Area?

3 Jing Ci Neo¹, Yihe Huang¹, Dongdong Yao¹, Shengji Wei²

4 [1] University of Michigan, Ann Arbor. 1100 North University, Room 4534F, neoj@umich.edu

5 [2] Asian School of the Environment, Nanyang Technological University. Earth Observatory of Singapore, 50
6 Nanyang Avenue, Block N2-01a-15

7
8 Questions can be directed to neoj@umich.edu

9 This paper is a preprint submitted to EarthArXiv. It has been accepted by the Bulletin of Seismological Society
10 America (BSSA) and is pending publication

11

12 **Abstract** The locations of aftershocks are often observed to be on the same fault plane as the
13 mainshock and used as proxies for its rupture area. Recent developments in earthquake relocation
14 techniques have led to great improvements in the accuracy of earthquake locations, offering an
15 unprecedented opportunity to quantify both the aftershock distribution and mainshock rupture
16 area. In this study, we design a consistent approach to calculate the area enclosed by aftershocks
17 of $M_w \geq 5.4$ mainshocks in California, normalized by the mainshock rupture area derived from
18 slip contours. We also investigate the Coulomb stress change from mainshock slip and compare it
19 to the aftershock zone. We find that overall, the ratios of aftershock zone area to mainshock rupture
20 area, hereinafter referred to as “aftershock ratio”, lie within a range of 0.5 to 5.4, with most values
21 larger than 1. Using different slip inversion models for the same mainshock can have a large impact
22 on the results, but the ratios estimated from both the relocated catalogs and Advanced National
23 Seismic System (ANSS) catalog have similar patterns. The aftershock ratios based on relocated
24 catalogs of Southern California fall between 0.5 and 4.3, while they exhibit a wider range from 1
25 to 5.4 for Northern California. Aftershock ratios for the early aftershock window (within 1 day)
26 show a similar range but smaller values than using the entire aftershock duration, and we propose
27 that continuing afterslip could contribute to the expanding aftershock zone area following several
28 mainshocks. Our results show that areas with positive Coulomb stress change scale with aftershock
29 zone areas, and spatial distribution of aftershocks represents stress release from mainshock rupture
30 and continuing postseismic slip.

31 **Introduction**

32 Beginning in the 1930s, scientists believed that aftershock zone area corresponds to the area where
33 strain is accumulated and released during an earthquake sequence (Utsu, 1969). However, large
34 uncertainty in earthquake location and the lack of slip models in early studies prevented scientists
35 from verifying this hypothesis (Das and Henry, 2003). With the advent of modern slip models and
36 large increase in the amount of seismic data, studies have qualitatively examined the aftershock

37 distribution of large earthquakes with respect to mainshock slip areas. They found that early
38 aftershocks (within the first 24 hours) tend to occur on the periphery of the eventual aftershock
39 zone, and the region in the center of the zone corresponds to the extent of the coseismic rupture
40 area (C. Mendoza and Hartzell, 1988; Dietz and Ellsworth, 1990; Oppenheimer, 1990; Das and
41 Henry, 2003). However, in spite of the wealth of literature on aftershock distribution, there has
42 been a dearth of studies that quantify the relationship between the aftershock zone area and the
43 mainshock rupture area, both immediately after the mainshock and over time. Recent
44 developments in seismological techniques have led to great improvements in the accuracy of
45 earthquake locations and finite fault solutions, and provided an unprecedented opportunity to
46 characterize the aftershock zone and the mainshock rupture using the latest earthquake catalogs
47 and slip models.

48 A better characterization of aftershock distribution is also the foundation for understanding the
49 underlying mechanisms of aftershock generation. Different mechanisms have been used to explain
50 the differences in aftershock distribution: static stress change, postseismic deformation, and
51 transient dynamic stress change (Freed, 2005). Transient dynamic stress change can be used to
52 account for earthquakes up to thousands of kilometers away (Belardinelli et al., 2003; Van Der
53 Elst and Brodsky, 2010; Parsons and Geist, 2014; Fan and Shearer, 2016), but due to the large
54 distances involved it is not relevant to this study. Static stress change is the stress change in the
55 earth's crust surrounding the fault planes due to slip on the faults (King et al., 1994, etc.). In
56 particular, Coulomb stress change became popular in the past few decades with numerous studies
57 attempting to correlate static Coulomb stress change with aftershocks (King et al., 1994; Stein et
58 al., 1997; Hardebeck et al., 1998; Toda et al., 1998, 2011; Kilb et al., 2002; Marsan and Lengliné,
59 2010, etc). Many of these studies found that the distribution of the aftershocks appears to be co-
60 located with regions of positive Coulomb stress change.

61 However, not all studies agree that static stress change is the only predictor of aftershock
62 distribution, especially the temporal evolution of aftershocks (Cattania et al., 2015). By
63 investigating over two hundred slip inversions, Meade et al. (2017) found that other stress change
64 components such as max shear stress and stress invariants, or postseismic deformation such as
65 afterslip/postseismic relaxation may account for the spatial distribution of aftershocks better. Both
66 afterslip and viscoelastic relaxation have been shown to be able to explain aftershock distribution
67 (Pollitz et al., 1998; Diao et al., 2014). For example, Perfettini and Avouac, (2004, 2007) found
68 that the aftershocks of the 1999 Chi-Chi earthquake and the 1992 Landers earthquake correlate
69 well with afterslip in both space and time. Savage et al., (2007) concluded that fault creep alone is
70 insufficient to explain the postseismic deformation and aftershocks of those earthquakes, thus
71 viscoelastic relaxation has to be considered.

72 In this study, we design a consistent approach to calculate the aftershock zone area and estimate
73 its relationship with the mainshock rupture area for both early aftershocks and the whole aftershock
74 duration. This approach applies the beta statistic (Matthews and Reasenberg, 1988) to provide a
75 more universal criterion to estimate the aftershock duration and aftershock boundary, which are
76 key factors in the calculation of the aftershock zone area and were previously determined upon
77 certain empirical assumptions. We select recent moderate to large ($M_w \geq 5.4$) mainshocks in
78 California that have both relocated aftershocks and resolved slip inversion models (Figure 1). To
79 further understand the aftershock generation mechanism, we also compute the static Coulomb
80 stress change from mainshock slip and compare it with the aftershock zone area. Meanwhile, we
81 compile published works on afterslip models and discuss their roles in modulating the aftershock
82 distribution.

83 **Data and Method**

84 We choose 12 moderate-to-large ($M_w \geq 5.4$) earthquakes in California as candidate mainshocks
85 (Figure 1). The slip inversion models are obtained from the Finite-Source Rupture Model Database
86 (SRCMOD) (see Data and Resources Section). We use both relocated catalog (either double-
87 difference or waveform relocated) and Advanced National Seismic System (ANSS) catalog for
88 following analysis. The relocated catalogs generally have better relative locations. However, a
89 certain percentage of earthquakes might be dropped during the relocation process and potentially
90 affect seismicity rate estimation. The ANSS catalog includes all archived earthquakes but endures
91 relatively larger location error. We include both catalogs to evaluate the consistency. More
92 specifically, the double-difference catalogs are acquired from the Northern California Earthquake
93 Data Center (NCEDC) (Waldhauser and Schaff, 2008; Waldhauser, 2009). Waveform relocated
94 catalogs are obtained from the Southern California Earthquake Data Center (SCEDC) (Hauksson
95 et al., 2012). We download earthquakes that occurred up to 1 year before and after each mainshock
96 within the surrounding area. We use an area that is deliberately much larger than needed to avoid
97 creating an artificial upper limit when calculating the aftershock zone area. A grid of ± 1 -degree
98 latitude and longitude relative to the mainshock epicenter is used to download earthquakes from
99 NCEDC/SCEDC, while a circle with a radius of five times the source dimension is used to
100 download earthquakes from the ANSS catalog.

101 *Earthquake Selection*

102 To choose earthquakes associated with mainshock faults, only earthquakes with off-fault distances
103 less than 2km to the fault plane from the slip inversion are kept for further analysis. We use 2km
104 because earthquake epicenter location uncertainties typically fall within 2km. We have tried
105 different off-fault distances from 1 to 20km and find that off-fault distances below 5km do not
106 show a large difference. As hypocenter locations given by the slip inversion data and the catalogs
107 are slightly different, we shift earthquake locations in the catalog using the hypocenter in the slip
108 inversion as a reference for some mainshocks. This ensures that the selection of earthquakes by

109 off-fault distance is accurate and does not affect the calculation of the aftershock zone area. The
110 fault planes are extrapolated past each end, and the earthquakes are then projected onto the nearest
111 fault plane (i.e., smallest fault-normal distance).

112 *Magnitude of Completeness*

113 To remove bias in calculating the change in seismicity rate, we need to ensure that the catalog is
114 complete for both the periods before and after the mainshock, i.e. there are no missing earthquakes
115 for the magnitude range we use. Hence, we calculate the magnitude of completeness (M_c) for both
116 time periods, and only earthquakes with magnitudes above the larger M_c are used. In a few cases,
117 M_c cannot be calculated for either before or after the mainshock, due to the sparsity of data or the
118 shape of the magnitude-frequency distribution (MFD). Hence, we use M_c of the time period that
119 can be calculated instead. The most straightforward way of calculating M_c is the maximum
120 curvature method, which often underestimates M_c for gradually curved bulk MFDs. The M_{c95}
121 and M_{c90} methods, which calculate the lowest M_c value that gives a best fit of 95% and 90%,
122 provide a closer estimate, but sometimes M_c cannot be calculated when the MFD curve never
123 reaches a 90% fit. Hence, we use the best combination method, whereby an initial estimate is
124 calculated using the max curve, and then the algorithm searches for the M_{c95} value and M_{c90}
125 value in a fixed range around the estimate. These methods are described thoroughly in Mignan and
126 Woessner (2012), and we use the open-source MATLAB code written by Schorlemmer and
127 Woessner (2004) to calculate M_c (see Data and Resources Section). We set the magnitude bin size
128 to be 0.1 and do not apply any correction.

129 *Beta Statistic: A measure of change in seismicity rate*

130 The β -statistic quantifies seismicity rate change based on the difference between the observed and
131 expected number of events occurring in a time period, normalized by the standard deviation of the
132 expected value (Kilb et al., 2000; Aron and Hardebeck, 2009). The standard deviation is calculated

133 by assuming a binomial distribution where earthquakes occur either inside or outside the time
134 period T_a (Matthews and Reasenberg, 1988). A β value of 2, which means 95% significance of
135 increase in seismicity when the β value is normalized by its standard deviation, is used as the
136 threshold to determine if there is a significant increase in seismicity. The equation to calculate the
137 β value is shown below (Equation 1).

$$138 \quad \beta = \frac{N_a - N * T_a / T}{\sqrt{N(T_a / T)(1 - T_a / T)}} \quad (1)$$

139 Where N_a is the number of events in the time period of interest, N is the number of events in the
140 entire time period, T_a is the duration of the time period of interest and T is the duration of the
141 entire time period (background window duration T_b plus above defined T_a).
142

143 ***Defining Aftershock Zone***

144 Determining aftershock zone area is difficult as aftershocks can occur over a large and continuous
145 area especially in places with high background seismicity such as Parkfield, and deciding which
146 earthquakes constitute aftershocks can be quite challenging. Methods used by previous studies
147 include fitting ellipses (Utsu, 1969), drawing energy contours (Tajima and Kanamori, 1985),
148 terminating the aftershock zone based on gaps between the earthquakes (Meng and Peng, 2016),
149 or drawing a simple boundary around the aftershocks (Sykes, 1971). We use the β -statistic to
150 calculate the aftershock zone area by defining the aftershock zone as the region with significant
151 increase in seismicity rate after the mainshock. To find the aftershock zone, we create a grid for
152 the fault plane and the surrounding regions and calculate the β value for each grid cell. A convex
153 boundary is then drawn around those areas with significant change in seismicity using the
154 MATLAB function “boundary” with a ‘shrink factor’ of 0, which is consistent with results using
155 Delaunay triangulation to denote the boundary. The area enclosed by the boundary is then taken
156 to be the aftershock zone area. Another possible method of calculating the aftershock area is to
157 add up area of cells with significant seismicity rate increase. However, we choose not to use this

158 method mainly because the aftershock zone area increases with cell size, which could be subjective
159 to provide a consistent way to estimate aftershock zone area spanning different magnitudes (Figure
160 S1). In comparison, drawing a boundary around the aftershocks is a robust way to define the
161 aftershock zone area that is largely unaffected by cell size (Table S1). Figure 2 illustrates the
162 calculation of the aftershock zone area. Previous calculations of β values have used different cell
163 sizes such as 2 km (Aron and Hardebeck, 2009) and 6 km (Kilb et al., 2000). As earthquakes are
164 represented as points in the grid, the choice of cell size has an impact on the β values. Using
165 different cell sizes that range from 1 to 4 km, we find that as long as the cell size is large enough
166 such that each earthquake is not isolated, the pattern of β values remains similar. However, a larger
167 cell size like 6 by 6 km (Kilb et al., 2000) is not appropriate as it is close to the rupture length of
168 the mainshock, which ranges from 9 to over 100 km in our analysis. Hence, we use a cell size of
169 2 by 2 km. We locate the areas where the β value is larger than 2 and terminate the aftershock
170 zone area when there is a gap larger than 15 km (Meng and Peng, 2016). We test a range of gap
171 sizes from 5 to 20 km and find that for small off-fault distances (≤ 5 km), and the gap size does not
172 affect the results.

173 The choice of time periods T and T_a (as in Equation 1) can greatly affect the calculation of the
174 aftershock zone area by controlling the number of earthquakes that constitute change in seismicity
175 rate. To estimate the background seismicity rate, we adopt a long-term averaged rate before the
176 mainshock. Previous studies reported obvious increasing foreshocks before some large
177 earthquakes (Dodge et al., 1995; Hauksson et al., 2002, etc). However, the short-term foreshock
178 activity should not significantly impact our calculation since we use a much longer window before
179 the mainshock. To test this, we use background window lengths of one year and two years and
180 find that the ratios are generally consistent except for the Whittier Narrows and North Palm Springs
181 earthquake (Figure S2). The range of ratios also remain the same using both pre-shock windows.
182 Since using a pre-shock duration of one year generates more consistent results between the

183 relocated and non-relocated catalogs, we use a pre-shock duration of one year to calculate β values
184 and aftershock zone areas.

185 ***Defining Aftershock Duration***

186 Scientists have previously pointed out that there was no formal agreement on a consistent space-
187 time windowing algorithm to select aftershocks (Knopoff et al., 1982), which is still true to this
188 date. The choice of aftershock duration is complicated by the fact that the aftershock zone area
189 could expand with time (Tajima and Kanamori, 1985), and different mechanisms could tangle
190 together with longer durations. Different aftershock durations ranging from one day (Kanamori,
191 1977), weeks (Wetzler et al., 2018) to years (Parsons, 2002; Perfettini and Avouac, 2007) have
192 been used, depending on the need of each study. Some studies suggested that earthquakes may still
193 have aftershocks decades or centuries later (Bouchon et al., 2013; Ebel and Chambers, 2016). Here
194 we define aftershock duration as the time period when there is still a significantly elevated rate of
195 seismicity in the region. We then calculate the sliding-window β value for the entire faulting
196 system (fault plane and the extended regions) using the aftershocks within an off-fault distance of
197 2km, with N in equation (1) equal to all the earthquakes that occurred in the region and T_a equal
198 to 10 days after the mainshock. We then slide the time window with a time interval of 5 days and
199 track the evolution of the β value through time. The entire aftershock duration is given by the first
200 time-window when the β value drops below the threshold value of 2. The aftershock duration gives
201 T_a , the time period of interest used in the calculation of the β value in each grid cell. The
202 aftershock duration can vary between a few weeks and over a year (Figure 3).

203 ***Aftershock Ratio***

204 The coseismic rupture area is defined as the area enclosed by a contour of 0.15 of the maximum
205 slip (Wetzler et al., 2018). A slip contour is used because areas with very low slip may not be well
206 resolved and depend greatly on the smoothing method used in the kinematic source inversion.

207 Hence, we also estimate the uncertainty from the slip models by calculating rupture areas with slip
208 contours of 0.1 and 0.2 of maximum slip. We then calculate the ratio of the aftershock zone area
209 to the coseismic rupture area to investigate how well the aftershock zone area approximates the
210 rupture area. Since each earthquake model is unique, some of them require special processing
211 procedures as listed in Table S2.

212 *Coulomb Stress Change Area*

213 In order to examine how the mainshock slip impacts the aftershock zone area, we utilize the
214 Coulomb 3 software to calculate the resulting Coulomb stress change of each earthquake (King et
215 al., 1994). We use the entire slip model and the orientation of the main fault plane as the receiver
216 fault to find the Coulomb stress change of the region. Assuming that earthquakes below a certain
217 off-fault distance lie on the same fault plane as the mainshock, we use the orientation of the main
218 fault plane as the receiver fault to find the Coulomb stress change of the region. We also use a
219 friction coefficient of 0.6, although faults have a large range of plausible values between 0 to 0.75
220 (King et al., 1994). The cross-section of the fault and its surrounding region are calculated with a
221 cell size of 1 by 1 km. We test thresholds of 0.1 and 1 MPa and find that both will result in a similar
222 trend, but the area enclosed by the 1 MPa cells are more similar to the aftershock zone area
223 observed from the β -statistic. Hence, we sum the area of the cells that have a positive Coulomb
224 stress change of 1 MPa or more to compare with the aftershock zone area (Figure 4). The results
225 of our Coulomb stress change calculations are listed in Table S3.

226 **Results**

227 We analyze a total number of 12 $M_w \geq 5.4$ California mainshocks (Table 1), with 3 events from
228 the NCEDC double-difference catalog and the rest from the SCEDC waveform relocated catalog.
229 Most of them are strike-slip events, except for the 1994 Northridge earthquake with a thrust
230 mechanism and the 1989 Loma Prieta earthquake with an oblique mechanism. We calculate the

231 aftershock ratio of each mainshock, often for multiple slip inversion models (Figure 5). The
232 parameters that we used are summarized in Table S4. We also list the data types used by each slip
233 model in Figure 5. Strong ground motion data are predominantly used for Northern California
234 (NC) earthquakes, while various data types are used for Southern California (SC) earthquakes.

235 We find that aftershock zone areas are within a range of 0.5 to 5.4 times of the mainshock rupture
236 area (Figure 6). Some earthquakes such as the 1989 Loma Prieta earthquake have consistently
237 higher ratios, while others such as the 1999 Hector Mine earthquake and the 1994 Landers
238 earthquake have consistently lower ratios. We explore their potential causes further in the
239 Discussion section. Ratios of the same earthquake estimated from different slip inversion models
240 can vary widely. For example, the ratio for the Gallovič (2016) model of the 2014 South Napa
241 earthquake is more than 3 times of the ratio for the Wei et al. (2015) model. This is partially
242 because the Wei et al. (2015) model has a slip area that is twice as large as the Gallovič (2016)
243 model. The two slip models also assume significantly different fault planes. Since only earthquakes
244 within 2km of the fault planes are included as potential aftershocks, the aftershock zone area
245 estimated for Wei's model is smaller than that for Gallovič's model. Our results also show a similar
246 pattern between the ratios estimated from the ANSS and relocated earthquake catalogs. Table 2
247 shows that both types of catalogs have almost identical average ratios, but the ANSS catalog has
248 larger variance. We also note that the ratios for 2012 Brawley and 1987 Elmore Ranch earthquakes
249 differ by a factor of 2 across the relocated and ANSS catalogs. The similar ratios estimated from
250 different catalogs demonstrate that aftershock zone area is a macroscopic source feature that is not
251 sensitive to the differences of earthquake locations in catalogs. We do not observe a clear
252 correlation between moment magnitudes and aftershock ratios either (Figure S3).

253 *Early Aftershock Zone*

254 Above results are based on the entire aftershock duration. Since different aftershock generation
255 mechanisms could affect the long-term aftershock evolution, we also measure ratios using only
256 early aftershocks to exclude postseismic deformation if existed. The early aftershock window is
257 set as 1-day after the mainshock (Kanamori, 1977) and the results are shown in Figure 7. Since the
258 T_a/T term is close to 0 in our study, every single earthquake in each cell after the mainshock would
259 be significant in the output beta value. Hence, only the off-fault distance, gap size and M_c are used
260 to determine which aftershocks to include in the analysis. Generally, the ratios for the 1-day
261 duration are smaller than or equal to those for the entire aftershock duration. But the range of ratios
262 (0.5-3.5) is comparable to the range for the entire aftershock duration (0.5-5.4). The early
263 aftershock ratios are listed in Table S5 and statistics of the ratios are shown in Table 2.

264 *Static Stress Change*

265 If aftershocks are primarily triggered by the Coulomb stress change, they should occur within the
266 area with the positive Coulomb stress change. Hence, we compare the positive Coulomb stress
267 change area and the aftershock zone area of each mainshock (Figure 3). We find that the Coulomb
268 stress change area shows a positive correlation with the aftershock zone area (Figure 8), which
269 may support the hypothesis of static stress change being a triggering mechanism for aftershocks.
270 However, this correlation does not necessarily mean causation. Alternatively, the correlation may
271 indicate that both static stress changes and aftershock areas are related to certain mainshock source
272 parameters. The correlation between the Coulomb stress change and the aftershock zone area is
273 not an ideal linear trend either, and the discrepancies may be due to the uncertainty from coseismic
274 slip models and the inclusion of other aftershock triggering mechanisms. In particular, the Loma
275 Prieta aftershock zone area appears to be an outlier, as its aftershock zone area is much larger than
276 that of the other earthquakes given its relatively small Coulomb stress change area. We also show
277 the ratio of Coulomb stress area to aftershock area with magnitude (Figure 9), and the results are

278 inconclusive, with either a slight increase or no change in ratio with magnitude depending on the
279 fitting method used.

280 **Discussion**

281 The value of the aftershock ratio can help reveal important characteristics of the region such as
282 aftershock mechanisms in play, but it cannot be used to precisely predict the mainshock rupture
283 area. One should be careful about drawing conclusions about the rupture area from the aftershock
284 zone area, as (1) there is a broad range of aftershock ratios, (2) even if the ratio is close to 1, the
285 spatial distribution of the aftershocks with respect to the mainshock rupture area may still be
286 different and (3) the aftershock ratios are based on California earthquakes and likely to differ even
287 more for earthquakes outside California. In this section, we discuss the potential causes of large
288 variations in aftershock ratios, including different aftershock mechanisms and uncertainties
289 introduced during our calculations. To further test the method, we also conduct similar analysis on
290 the 2011 Virginia earthquake outside California. Given the large difference in crustal structure
291 between California and the eastern U.S., the Virginia earthquake serves as an extreme contrast to
292 California earthquakes.

293 *Comparison to a non-California earthquake: An example from the Eastern U.S.*

294 We analyze the 23 August 2011 M5.7 Mineral, Virginia earthquake using the slip model from
295 Chapman (2013) and double-difference relocated earthquakes from Wu et al. (2015). We do not
296 use the ANSS catalog that has very few earthquakes over two years (~54). Since the double-
297 difference catalog only has earthquakes starting from 25th August 2011, we cannot calculate
298 aftershock duration, 1-day aftershock zone area or M_c of the background seismicity. Here we
299 assume an aftershock duration of one year and obtain an aftershock ratio of 14.1 for aftershocks
300 within an off-fault distance of 2 km (Figure S4). The ratio of the aftershock zone area to the
301 Coulomb stress change area is 14.3. Since the result is subject to the unknown M_c and uncertainty

302 in aftershock duration, we also investigate their effects by varying M_c in the range of 0 and 1 (the
303 catalog has an M_c of 0) and changing aftershock durations between 5 and 365 days. We find that
304 the aftershock ratio is still much larger than the ratios we obtained for the Californian earthquakes.
305 The aftershock ratio of 14.1 for the Virginia earthquake is ~ 3 –28 times as large as the ratios we
306 obtained for Californian earthquakes, and the disparity cannot be explained by Coulomb stress
307 change. One possible reason for the large aftershock ratio may be because of the unusually high
308 stress drops of the mainshock (Wu and Chapman, 2017). The high stress drop may have led to a
309 smaller rupture area than California earthquakes with the same magnitude, while the aftershock
310 zone area remains typical for a $M_{5.7}$ mainshock. This example suggests that aftershock ratios may
311 depend heavily upon tectonic environment and the resulting differences in earthquake
312 characteristics.

313 *Afterslip: An alternative aftershock mechanism*

314 As Coulomb stress change cannot satisfactorily explain the large aftershock zone area of the Loma
315 Prieta mainshock, an alternative mechanism for aftershock generation is afterslip following the
316 mainshock. The variation of geologic conditions in California results in different amounts of
317 afterslip for each earthquake. The central part of the San Andreas Fault exhibits large amounts of
318 aseismic creep (Khoshmanesh and Shirzaei, 2018), whereas the southern portion is locked with
319 significant slip deficit (Fialko, 2006). Though the underlying reason is not well known, some
320 studies suggest that it might be due to the presence of serpentinite at creeping faults in Northern
321 and Central California (Moore and Rymer, 2007). Studies have shown that the Loma Prieta
322 earthquake has afterslip extending around 40-60km towards the southeast along the San Andreas
323 fault (Behr et al., 1990; Pollitz et al., 1998). The shallow afterslip (above 15km depth) was found
324 to have most likely occurred on the Loma Prieta fault (Bürgmann et al., 1997). Although the
325 afterslip was found to be relatively small (less than 1 cm over 4 months), the afterslip area roughly

326 corresponds to the aftershock zone area in our analysis, which extends southwards for 60 km from
327 the mainshock rupture in a shallow region above 15 km depth. Hence, we argue that the afterslip
328 could account for the large aftershock zone area of Loma Prieta.

329 Afterslip can occur in the surrounding region loaded by mainshock rupture and transfer stresses
330 on faults that promote the generation of aftershocks. It is unfeasible to quantitatively evaluate the
331 contribution by Coulomb stress change and other mechanisms without detailed rupture simulation
332 based on realistic parameters. For mainshocks with observed afterslip, a combination of the static
333 stress change and afterslip instead of the Coulomb stress change alone could contribute to the
334 positive correlation between the Coulomb stress change area and the aftershock zone area. By
335 comparing the ratios from using both entire aftershock duration (Figure 6) and early aftershocks
336 (Figure 7), we observe that the long-term aftershock duration results in relatively larger ratio for
337 the South Napa, Loma Prieta, Brawley, Joshua Tree, Elmore Ranch and Whittier Narrows
338 earthquakes. The larger ratio could be explained by expanding aftershock zones with time caused
339 by postseismic deformation process. In contrast, similar range of aftershock ratios for the other
340 earthquakes support that Coulomb stress change caused by the mainshock rupture plays an
341 important role in aftershock distribution.

342 We also search for published work on postseismic slip following the studied mainshocks, and
343 seven earthquakes have resolved postseismic slip model (Table S6). For most earthquakes
344 analyzed in the table, the afterslip distribution is similar in extent to our aftershock zone area
345 though their depths may be different, which is consistent with emerging evidences that afterslip
346 could affect the long-term aftershock evolution (Perfettini et al., 2018). To better understand the
347 outlier mainshocks, we could potentially use afterslip models to measure the stress change caused
348 by afterslip, similar to that of Perfettini and Avouac (2004; 2007), to ascertain if it correlates better
349 with their aftershock zone areas. This exceeds the scope of this study and could be a potential work
350 in future with more available afterslip models.

351 *Uncertainty and Limitations*

352 The measurement uncertainties in our calculations include the (1) earthquakes locations, (2) the
353 calculation of M_c , (3) the assumption of threshold β value, (4) the upper limit of the grid and gap
354 size, (5) slip inversion results, and (6) the assumption that the fault plane extends in roughly the
355 same plane outside of the mainshock rupture area.

356 As shown by the large variations of ratios for different slip models, slip inversion results probably
357 contribute to the largest uncertainty in this study. Thus, we estimate the uncertainty by calculating
358 rupture areas defined by 0.1 and 0.2 of the maximum slip (Table S7), which is shown as error bars
359 in Figures 6 and 7. The results show that the aftershock ratios of 2014 South Napa and 1986 North
360 Palm Springs earthquakes may be biased by slip models that have large uncertainty. Aside from
361 the slip contours, other sources of error from the slip models include the slip inversion parameters
362 used, such as the geometry and orientation of the fault planes, but they are much harder to quantify.

363 We also examined the uncertainty of earthquake locations for the Parkfield mainshock using the
364 Ji (2004) model. We use location uncertainties of 0.5km, 1km and 2km to randomly vary the
365 locations of all the aftershocks. We generate 10,000 synthetic distributions of aftershocks and find
366 the standard deviations of aftershock zone areas are 0.09, 0.12 and 0.15 respectively, which is
367 about 4.8 to 7.8% of the mean value. As the location uncertainties for most earthquakes are smaller
368 than 2km, we believe that the location uncertainty will not greatly affect the ratios.

369 We calculate M_c before and after the mainshock and remove earthquakes below M_c . Though this
370 procedure ensures that the seismicity change is not biased by the incomplete catalog, it also
371 removes earthquakes from consideration, which may cause the calculated aftershock zone area to
372 be smaller than the real aftershock zone area. To estimate the impact of removing earthquakes
373 below M_c , we calculate the aftershock zone areas of the Brawley and El Mayor-Cucapah
374 mainshocks using the Quake Template Matching (QTM) Catalog for Southern California (Ross et

375 al., 2019) that has a much lower M_c due to the new detections. The ratios of aftershock zone areas
376 to mainshock rupture areas estimated from this catalog are larger than that calculated from the
377 relocated SCEDC catalog (Table S8, Figure S5). However, they are still within the range of ratios
378 (0.5-5.4) obtained for all the mainshocks.

379 We limit the calculation of the aftershock zone area by setting a threshold β value of 2. A threshold
380 value of 2 indicates 95% significance of increase in seismicity when we normalize the β value by
381 its standard deviation. The assumption behind the calculation of standard deviation is that each
382 earthquake is an independent event and the probability of an earthquake occurring at any given
383 time is equal. This may not be a valid assumption for earthquakes as the probability of having
384 earthquakes after a mainshock is much higher than before the mainshock, but all metrics for
385 determining aftershock zone area necessarily contain arbitrariness.

386 We also set an upper limit of the spatial grid and gap to terminate aftershock zone, which is many
387 times of the source dimension but may still violate the observation of the so-called “global
388 aftershock zone” (Parsons and Geist, 2014; Johnson and Bürgmann, 2016). Among our
389 investigated mainshocks, we noticed an increase of microearthquakes within the Geysers
390 geothermal region following the 2014 Napa earthquake (Figure 2), likely triggered by the passing
391 seismic waves (Meng et al., 2014). More recently, Ross et al. (2019) suggested that the 2010 El
392 Mayor-Cucapah earthquake widely triggered events in Southern California. Hence, we are
393 referring to the traditional aftershock zone in this study, where various triggering mechanisms are
394 comparable.

395 ***Other Results***

396 Studies have shown that aftershocks tend to be concentrated around the boundary of the mainshock
397 rupture zone, with a deficit in the center regions of higher slip (Carlos Mendoza and Hartzell, 1988;
398 Dietz and Ellsworth, 1990; Wetzler et al., 2018). This is because most of the strain in the regions

399 of higher slip are already released during the mainshock and hence these areas are less able to
400 generate aftershocks. We test this hypothesis using a slightly modified version of the method used
401 in Wetzler et al. (2018), which calculates the distances of aftershocks from the slip contours of
402 several earthquakes and normalizes by the radius of a circle that has an area equal to the area
403 enclosed by the slip contour. As many of our slip contours are elongated, we change the
404 normalization constant to the minor axis of an ellipse fitted to the slip contours (Wijewickrema
405 and Paplinski, 2004), as shown in Figure 10. The distances are then calculated from the closest
406 slip contour (if there are multiple parts) and normalized by the minor axis of the ellipse fitted to
407 that slip contour. Negative distances refer to distances of aftershocks inside the slip contour while
408 positive distances refer to distances of aftershocks outside the slip contour. We use this method to
409 analyze one slip model from each earthquake (list of models in Table S9). We find that most of
410 the aftershocks are located near the slip contours, within a distance of -0.25 to 0.25 the slip
411 contours. Compared to the results obtained by Wetzler et al. (2018), we find more earthquakes
412 located between 0.5 to 1 distance inside the slip contours (Figure 11), probably because we use the
413 minor axis of an ellipse as the normalization constant. But our results still support the notion that
414 there is a deficit of earthquakes in the central regions of the largest slip.

415 **Conclusion**

416 We have developed a consistent method to quantify aftershock zone and mainshock rupture areas,
417 and analyzed 12 mainshocks ($M_w \geq 5.4$) in California. We find that the ratios of aftershock zone
418 areas to mainshock rupture areas lie within a range of 0.5 to 5.4, and can be used as a first order
419 estimate of the mainshock rupture area, especially for early aftershock durations where ratios range
420 from 0.5 to 3.5. Using either the relocated catalog or the ANSS catalog leads to similar patterns of
421 the aftershock zone area. Our results show that Coulomb stress change exhibits a positive
422 correlation with aftershock zone area, suggesting that the mainshock slip contributes to aftershock

423 distribution. Moreover, a combination of different mechanisms should be used to better explain
424 the aftershock zone areas (especially for the entire aftershock duration) for several mainshocks.
425 Further studies should be directed towards understanding how the relationship between the
426 aftershock zone area and the mainshock rupture area varies for earthquakes in different tectonic
427 environments and crustal structures.

428 Data and Resources

429 Slip inversion data was downloaded from the SRCMOD website at <http://equake-rc.info> (last
430 accessed July 2020). Earthquake catalogs were obtained from the NCEDC www.ncedc.org (last
431 accessed October 2019) and SCEDC websites <http://scedc.caltech.edu> (last accessed October
432 2019) and the catalog by Dr. Felix Waldhauser,
433 <https://www.ldeo.columbia.edu/~felixw/NCAeqDD/> (last accessed March 2019), version
434 NCAeqDD.v201112.1. Earthquakes from the ANSS ComCat Catalog were downloaded from
435 USGS <https://earthquake.usgs.gov/earthquakes/search/> (last accessed August 2019) and Coulomb
436 3 MATLAB codes were downloaded from the USGS website,
437 <https://earthquake.usgs.gov/research/software/coulomb/> (last accessed July 2019). We obtained
438 MATLAB codes written by D. Schorlemmer and J. Woessner to calculate M_c from
439 geophysics.eas.gatech.edu/people/bsullivan/tutorial/StatisticalSeismology.htm (last accessed
440 March 2019). The supplementary material contains additional information about individual
441 earthquakes, early aftershock ratios and the results of Coulomb stress change calculations.

442 Acknowledgements

443 We thank two anonymous reviewers and editors Martin C. Chapman and Thomas Pratt for their
444 insightful feedback for this paper. We also thank the CN Yang Scholars Program, Nanyang
445 Technological University, and the University of Michigan for supporting the undergraduate
446 research study of Jing Ci Neo. We would also like to express appreciation to Carissa Tan Xiwen

447 for reviewing this paper. Jing Ci Neo and Yihe Huang acknowledge the funding support from the
448 National Science Foundation through grant award 1943742.

449
450 **References**

- 451
452 Aron, A., and J. L. Hardebeck, 2009, Seismicity rate changes along the central California coast due to stress changes
453 from the 2003 M 6.5 San Simeon and 2004 M 6.0 Parkfield earthquakes, *Bull. Seismol. Soc. Am.*, doi:
454 10.1785/0120080239.
- 455 Behr, J., R. Bilham, P. Bodin, R. O. Burfoid, and R. Bürgmann, 1990, Aseismic slip on the San Andreas Fault south
456 of Loma Prieta, *Geophys. Res. Lett.*, doi: 10.1029/GL017i009p01445.
- 457 Belardinelli, M. E., A. Bizzarri, and M. Cocco, 2003, Earthquake triggering by static and dynamic stress changes, *J.*
458 *Geophys. Res. Solid Earth*, 108, no. B3, 2135, doi: 10.1029/2002jb001779.
- 459 Bennett, R. A., R. E. Reilinger, W. Rodi, Y. P. Li, M. N. Toksoz, and K. Hudnut, 1995, Coseismic Fault Slip
460 Associated with the 1992 M(W)-6.1 Joshua-Tree, California, Earthquake – Implications for the Joshua-
461 Tree Landers Earthquake Sequence, *J. Geophys. Res.*, 100, no. B4, 6443–6461
- 462 Bouchon, M., V. Durand, D. Marsan, H. Karabulut, and J. Schmittbuhl, 2013, The long precursory phase of most
463 large interplate earthquakes, *Nat. Geosci.*, 6, 299–302, doi: 10.1038/ngeo1770.
- 464 Bürgmann, R., P. Segall, M. Lisowski, and J. L. Svarc, 1997, Postseismic strain following the Loma Prieta
465 earthquake from repeated GPS measurements, *J. Geophys. Res.*, 102, no. B3, 4933–4955.
- 466 Cattania, C., S. Hainzl, L. Wang, B. Enescu, and F. Roth, 2015, Journal of Geophysical Research : Solid Earth
467 Aftershock triggering by postseismic stresses : A study based on Coulomb rate-and-state models, *J. Geophys.*
468 *Res. Solid Earth*, 120, 2388–2407, doi: 10.1002/2014JB011500.The.
- 469 Chapman, M. C., 2013, On the Rupture Process of the 23 August 2011 Virginia Earthquake, *Bull. Seism. Soc. Am.*,
470 103, no. 2A, 613–628.
- 471 Cotton, F., and M. Campillo, 1995, Frequency-Domain Inversion of Strong Motions - Application to the 1992
472 Landers Earthquake, *J. Geophys. Res.*, 100, no. B3, 3961–63975.
- 473 Custodio, S., P. C. Liu, and R. J. Archuleta, 2005, The 2004 Mw 6.0 Parkfield, California, earthquake: Inversion of
474 near-source ground motion using multiple data sets, *Geophys. Res. Lett.*, 32, no. L23312.
- 475 Das, S., and C. Henry, 2003, Spatial relation between main earthquake slip and its aftershock distribution, *Rev.*
476 *Geophys.*, 41, no. 3.
- 477 Diao, F., X. Xiong, R. Wang, Y. Zheng, T. R. Walter, H. Weng, and J. Li, 2014, Overlapping post-seismic
478 deformation processes: Afterslip and viscoelastic relaxation following the 2011Mw 9.0 tohoku (Japan)
479 earthquake, *Geophys. J. Int.*, 196, 218–229, doi: 10.1093/gji/ggt376.
- 480 Dietz, L. D., and W. L. Ellsworth, 1990, The October 17, 1989, Loma Prieta, California, Earthquake and its
481 aftershocks: Geometry of the sequence from high-resolution locations, *Geophys. Res. Lett.*, doi:
482 10.1029/GL017i009p01417.
- 483 Dodge, D. A., G. C. Beroza, and W. L. Ellsworth, 1995, Foreshock sequence of the 1992 Landers, California,
484 earthquake and its implications for earthquake nucleation, *J. Geophys. Res.*, 100, no. B7, 9865–9880, doi:
485 10.1029/95JB00871.
- 486 Dreger, D. S., L. Gee, P. Lombard, M. H. Murray, and B. Romanowicz, 2005, Rapid finite-source analysis and near-
487 fault strong ground motions: Application to the 2003 M-w 6.5 San Simeon and 2004 Mw 6.0 Parkfield
488 earthquakes, *Seismol. Res. Lett.*, 76, no. 1, 40–48.
- 489 Ebel, J. E., and D. W. Chambers, 2016, Using the locations of $M \geq 4$ earthquakes to delineate the extents of the
490 ruptures of past major earthquakes, *Geophys. J. Int.*, 2, no. 1, 862–875 doi: 10.1093/gji/ggw312.
- 491 Emolo, A., and A. Zollo, 2005, Kinematic Source Parameters for the 1989 Loma Prieta Earthquake from the
492 Nonlinear Inversion of Accelerograms, *Bull. Seism. Soc. Am.*, 95, no. 3, 981–994.
- 493 Fan, W., and P. M. Shearer, 2016, Local near instantaneously dynamically triggered aftershocks of large
494 earthquakes, *Geophysics*, 353, no. 6304, 1133–1136.
- 495 Fialko, Y., 2006, Interseismic strain accumulation and the earthquake potential on the southern San Andreas fault
496 system, *Nature*, 441, 968–971, doi: 10.1038/nature04797.
- 497 Freed, A. M., 2005, Earthquake triggering by static, dynamic, and postseismic stress transfer, *Annu. Rev. Earth*
498 *Planet. Sci.*, 33, no. October 1999, 335–367, doi: 10.1146/annurev.earth.33.092203.122505.
- 499 Gallovič, F., 2016, Modeling velocity recordings of the mw 6.0 south napa, California, earthquake: Unilateral event
500 with weak high-frequency directivity, *Seismol. Res. Lett.*, 87, no. 1, 2–14, doi: 10.1785/0220150042.
- 501 Hardebeck, J. L., J. J. Nazareth, and E. Hauksson, 1998, The static stress change triggering model: Constraints from
502 two southern California aftershock sequences, *J. Geophys. Res.*, 103, no. B10, 24,427-24,437.

- 503 Hartzell, S., 1989, Comparison of Seismic Waveform Inversion Results for the Rupture History of a Finite Fault -
504 Application to the 1986 North Palm-Springs, California, Earthquake, *J. Geophys. Res.*, 94, no. B6, 7515–
505 7534.
- 506 Hartzell, S. H., and M. Iida, 1990, Source complexity of the 1987 Whittier Narrows, California, earthquake from
507 the inversion of strong motion records, *J. Geophys. Res.*, 95, no. 8, 12,475–12,485.
- 508 Hauksson, E., L. M. Jones, and K. Hutton, 2002, The 1999 Mw 7.1 Hector Mine, California, earthquake sequence:
509 Complex conjugate strike-slip faulting, *Bull. Seismol. Soc. Am.*, 92, no. 4, 1154–1170, doi:
510 10.1785/0120000920.
- 511 Hauksson, E., W. Yang, and P. M. Shearer, 2012, Waveform relocated earthquake catalog for Southern California
512 (1981 to June 2011), *Bull. Seismol. Soc. Am.*, 102, no. 5, 2239–2244, doi: 10.1785/0120120010.
- 513 Hernandez, B., F. Cotton, and M. Campillo, 1999, Contribution of radar interferometry to a two-step inversion of
514 the kinematic process of the 1992 Landers earthquake, *J. Geophys. Res.*, 104, no. B6, 13083–13099.
- 515 Ji, C., 2004, Slip history the 2004 (Mw 5.9) Parkfield Earthquake (Single-Plane Model), Caltech:
516 <http://www.tectonics.caltech.edu/slip_history/2004_ca/parkfield2.html> (accessed Mar 26, 2019).
- 517 Johnson, C. W., and R. Bürgmann, 2016, Delayed dynamic triggering: Local seismicity leading up to three remote
518 $M \geq 6$ aftershocks of the 11 April 2012 M8.6 Indian Ocean earthquake, *J. Geophys. Res. Solid Earth*, 121,
519 134–151, doi: 10.1002/2015JB012608.Received.
- 520 Jonsson, S., H. Zebker, P. Segall, and F. Amelung, 2002, Fault slip distribution of the 1999 Mw 7.1 Hector Mine,
521 California, earthquake, estimated from satellite radar and GPS measurements, *Bull. Seis. Soc. Am*, 92, no.
522 4, 1377–1389.
- 523 Kanamori, H., 1977, The energy release in great earthquakes, *J. Geophys. Res.*, 82, no. 20, 2981–2987, doi:
524 10.1029/jb082i020p02981.
- 525 Kaverina, A., D. Dreger, and E. Price, 2002, The combined inversion of seismic and geodetic data for the source
526 process of the 16 October 1999 Mw 7.1 Hector Mine, California, earthquake, *Bull. Seism. Soc. Am*, 92,
527 no. 4, 1266–1280.
- 528 Khoshmanesh, M., and M. Shirzaei, 2018, Episodic creep events on the San Andreas Fault caused by pore pressure
529 variations, *Nat. Geosci.*, 11, no. 8, 610–614, doi: 10.1038/s41561-018-0160-2.
- 530 Kilb, D., J. Gomberg, and P. Bodin, 2002, Aftershock triggering by complete Coulomb stress changes, *J. Geophys.*
531 *Res. Solid Earth*, 107, no. B4, 2060, doi: 10.1029/2001jb000202.
- 532 Kilb, D., J. Gomberg, and P. Bodin, 2000, Triggering of earthquake aftershocks by dynamic stresses, *Nature*, 408,
533 570–574.
- 534 King, G. C. P., R. S. Stein, and Jian Lin, 1994, Static stress changes and the triggering of earthquakes, *Bull.*
535 *Seismol. Soc. Am.*, 84, no. 3, 935–953, doi: 10.1016/0148-9062(95)94484-2.
- 536 Knopoff, L., Y. Y. Kagan, and R. Knopoff, 1982, b Values for Foreshocks and Aftershocks in Real and Simulated
537 Earthquake Sequences, *Bull. Seismol. Soc. Am.*, 72, no. 5, 1663–1676.
- 538 Larsen, S., R. Reilinger, H. Neugebauer, and W. Strange, 1992, Global Positioning System Measurements of
539 Deformations Associated with the 1987 Superstition Hills Earthquake – Evidence for Conjugate Faulting,
540 *J. Geophys. Res.*, 97, no. B4, 4885–4902.
- 541 Marsan, D., and O. Lengliné, 2010, A new estimation of the decay of aftershock density with distance to the
542 mainshock, *J. Geophys. Res. Solid Earth*, 115, no. B09302, doi: 10.1029/2009JB007119.
- 543 Matthews, M. V., and P. A. Reasenber, 1988, Statistical methods for investigating quiescence and other temporal
544 seismicity patterns, *Pure Appl. Geophys.*, 126, nos. 2–4, 357–372, doi: 10.1007/BF00879003.
- 545 Meade, B. J., P. M. R. DeVries, J. Faller, F. Viegas, and M. Wattenberg, 2017, What Is Better Than Coulomb
546 Failure Stress? A Ranking of Scalar Static Stress Triggering Mechanisms from 105 Mainshock-Aftershock
547 Pairs, *Geophys. Res. Lett.*, doi: 10.1002/2017GL075875.
- 548 Mendoza, C., and S. H. Hartzell, 1988, Aftershock patterns and main shock faulting, *Bull. Seismol. Soc. Am.*, 78,
549 no. 4, 1438–1449.
- 550 Mendoza, Carlos, and S. H. Hartzell, 1988, Inversion for Slip Distribution Using Teleseismic P Waveforms: North
551 Palm Springs, Borah Peak and Michocan Earthquakes, *Bull. Seismol. Soc. Am.*, 78, no. 3, 1092–1111.
- 552 Meng, X., and Z. Peng, 2016, Increasing lengths of aftershock zones with depths of moderate-size earthquakes on
553 the San Jacinto Fault suggests triggering of deep creep in the middle crust, *Geophys. J. Int.*, doi:
554 10.1093/gji/ggv445.
- 555 Meng, X., Z. Peng, C. Aiken, and D. Kilb, 2014, Dynamically Triggered Earthquakes in the Geysers Region
556 following the 2014 M6.0 South Napa Earthquake, *Eos AGU Fall Meet.*
- 557 Mignan, A., and J. Woessner, 2012, Estimating the magnitude of completeness for earthquake catalogs, *Community*
558 *Online Resource for Statistical Seismicity Analysis*, *Community Online Resour. Stat. Seism. Anal.*, doi:
559 10.5078/corssa-00180805.
- 560 Moore, D. E., and M. J. Rymer, 2007, Talc-bearing serpentinite and the creeping section of the San Andreas fault,
561 *Nature*, 448, 795–797, doi: 10.1038/nature06064.
- 562 Oppenheimer, D. H., 1990, Aftershock Slip Behavior of the 1989 Loma California Earthquake, *Geophys. Res. Lett.*,

563 17, no. 8, 1199–1202.

564 Parsons, T., 2002, Global Omori law decay of triggered earthquakes: Large aftershocks outside the classical
565 aftershock zone, *J. Geophys. Res. Solid Earth*, 107, no. B9, 2199, doi: 10.1029/2001jb000646.

566 Parsons, T., and E. L. Geist, 2014, The 2010–2014.3 global earthquake rate increase, *Geophys. Res. Lett.*, 41, 4479–
567 4485, doi: 10.1002/2014GL061184. Received.

568 Perfettini, H., and J. P. Avouac, 2007, Modeling afterslip and aftershocks following the 1992 Landers earthquake, *J.*
569 *Geophys. Res. Solid Earth*, doi: 10.1029/2006JB004399.

570 Perfettini, H., and J.-P. Avouac, 2004, Postseismic relaxation driven by brittle creep: A possible mechanism to
571 reconcile geodetic measurements and the decay rate of aftershocks, application to the Chi-Chi earthquake,
572 Taiwan, *J. Geophys. Res. Solid Earth*, 109, no. B02304, doi: 10.1029/2003jb002488.

573 Perfettini, H., W. B. Frank, D. Marsan, and M. Bouchon, 2018, A Model of Aftershock Migration Driven by
574 Afterslip, *Geophys. Res. Lett.*, 45, 2283–2293, doi: 10.1002/2017GL076287.

575 Pollitz, F. F., R. Bürgmann, and P. Segall, 1998, Joint estimation of afterslip rate and postseismic relaxation
576 following the 1989 Loma Prieta earthquake, *J. Geophys. Res. Solid Earth*, 103, no. B11, 26,975–26,992, doi:
577 10.1029/98jb01554.

578 Ross, Z. E., D. T. Trugman, E. Hauksson, and P. M. Shearer, 2019, Searching for hidden earthquakes in Southern
579 California, *Science* (80-.), 364, 767–771, doi: 10.1126/science.aaw6888.

580 Savage, J. C., J. L. Svarc, and S. B. Yu, 2007, Postseismic relaxation and aftershocks, *J. Geophys. Res. Solid Earth*,
581 112, no. B06406, doi: 10.1029/2006JB004584.

582 Stein, R. S., A. A. Barka, and J. H. Dieterich, 1997, Progressive failure on the North Anatolian fault since 1939 by
583 earthquake stress triggering, *Geophys. J. Int.*, 127, 594–604.

584 Sykes, L. R., 1971, Aftershock zones of great earthquakes, seismicity gaps, and earthquake prediction for Alaska
585 and the Aleutians, *J. Geophys. Res.*, 76, no. 32, 8021–8041, doi: 10.1029/jb076i032p08021.

586 Tajima, F., and H. Kanamori, 1985, Global survey of aftershock area expansion patterns, *Phys. Earth Planet. Inter.*,
587 doi: 10.1016/0031-9201(85)90066-4.

588 Toda, S., R. S. Stein, and J. Lin, 2011, Widespread seismicity excitation throughout central Japan following the
589 2011 M=9.0 Tohoku earthquake and its interpretation by Coulomb stress transfer, *Geophys. Res. Lett.*, 38, no.
590 L00G03, doi: 10.1029/2011GL047834.

591 Toda, S., R. S. Stein, P. a Reasenber, and H. Dieterich, 1998, Stress transferred by the 1995 Mw = 6.9 Kobe, Japan,
592 shock: Effect on aftershocks and future earthquake probabilities, *J. Geophys. Res.*, 103, no. B10, 24,543–24,
593 565.

594 Utsu, T., 1969, Instructions for use Aftershocks and Earthquake Statistics (I), *J. Fac. Sci. Hokkaido Univ.*, 3, no. 3,
595 129–195.

596 Van Der Elst, N. J., and E. E. Brodsky, 2010, Connecting near-field and far-field earthquake triggering to dynamic
597 strain, *J. Geophys. Res.*, 115, no. B07311, doi: 10.1029/2009JB006681.

598 Wald, D. J., D. V. Helmberger, and T. H. Heaton, 1991, Rupture Model of the 1989 Loma-Prieta Earthquake from
599 the Inversion of Strong-Motion and Broad-Band Teleseismic Data, *Bull. Seism. Soc. Am*, 81, no. 5, 1540–
600 1572.

601 Wald, D. J., T. H. Heaton, and K. W. Hudnut, 1996, The slip history of the 1994 Northridge, California, earthquake
602 determined from strong-motion, teleseismic, GPS, and leveling data, *Bull. Seism. Soc. Am*, 86, 1B, S49–
603 S70.

604 Waldhauser, F., 2009, Near-real-time double-difference event location using long-term seismic archives, with
605 application to northern California, *Bull. Seismol. Soc. Am.*, 99, no. 5, 2736–2748, doi: 10.1785/0120080294.

606 Waldhauser, F., and D. P. Schaff, 2008, Large-scale relocation of two decades of Northern California seismicity
607 using cross-correlation and double-difference methods, *J. Geophys. Res. Solid Earth*, 113, no. B08311, doi:
608 10.1029/2007JB005479.

609 Wei, S., D. V. Helmberger, S. Owen, R. W. Graves, K. W. Hudnut, and E. Fielding, 2013, Complementary slip
610 distributions of the largest earthquakes in the 2012 Brawley swarm, Imperial Valley, California. *Geophys.*
611 *Res. Lett.*, 40, 847–852, doi:10.1002/grl.50259.

612 Wei, S., E. Fielding, S. Leprince, A. Sladen, J. P. Avouac, D. Helmberger, E. Hauksson, R. Chu, M. Simons, K.
613 Hudnut, T. Herring, and R. Briggs, 2011, Superficial simplicity of the 2010 El Mayor-Cucapah earthquake
614 of Baja California in Mexico, *Nat. Geosci.*, 4, 615–618, doi:10.1038/ngeo1213.

615 Wei, S., S. Barbot, R. Graves, J. J. Lienkaemper, T. Wang, K. Hudnut, Y. Fu, and D. Helmberger, 2015, The 2014
616 Mw 6.1 South Napa Earthquake: A unilateral rupture with shallow asperity and rapid afterslip, *Seismol. Res.*
617 *Lett.*, 86, no. 2A, 344–354, doi: 10.1785/0220140249.

618 Wetzler, N., T. Lay, E. E. Brodsky, and H. Kanamori, 2018, Systematic deficiency of aftershocks in areas of high
619 coseismic slip for large subduction zone earthquakes, *Sci. Adv.*, doi: 10.1126/sciadv.aao3225.

620 Wijewickrema, S. N. R., and A. P. Paplinski, 2004, Principal Component Analysis for the Approximation of a Fruit
621 as an Ellipse.

622 Wu, Q., and M. C. Chapman, 2017, Stress-Drop Estimates and Source Scaling of the 2011 Mineral, Virginia,

623 Mainshock and Aftershocks, *Bull. Seism. Soc. Am*, 107, no. 6, 2703–2720.
624 Wu, Q., M. C. Chapman, and J. N. Beale, 2015, The Aftershock Sequence of the 2011 Mineral, Virginia,
625 Earthquake: Temporal and Spatial Distribution, Focal Mechanisms, Regional Stress, and the Role of Coulomb
626 Stress Transfer, *Bull. Seism. Soc. Am*, 105, no. 5, 2521–2537.
627 Zeng, Y., and J. Anderson, 2000, Evaluation of numerical procedures for simulating near-fault long-period ground
628 motions using Zeng method, Report 2000/01 to the PEER Utilities Program, Berkeley:
629 <<http://peer.berkeley.edu>> (accessed March 23, 2019).
630
631

632 **Full Mailing Addresses of Authors**

633

634 Jing Ci Neo

635 University of Michigan, Ann Arbor. Room 4534F, 1100 North University

636

637 Yihe Huang

638 University of Michigan, Ann Arbor. Room 4534F, 1100 North University

639

640 Dongdong Yao

641 University of Michigan, Ann Arbor. Room 4534F, 1100 North University

642

643 Shengji Wei

644 Earth Observatory of Singapore, 50 Nanyang Avenue, Block N2-01a-15

645

646

647 **List of Figure Captions**

- 648
649 **Figure 1.** Map of mainshock locations in this study. Known faults are specified as dark red lines, and the
650 direction of plate motion is indicated by black arrows.
651
- 652 **Figure 2.** Illustration of how the aftershock zone area of each mainshock is defined using the β values. The
653 diagrams show the fault plane view, with β values of each grid cell calculated from the aftershocks
654 projected on to the fault plane. Aftershocks from the relocated catalogs are used for this figure.
655
- 656 **Figure 3.** Illustration of how aftershock duration is calculated. The horizontal black line is at a β value of
657 2, and the aftershock duration is taken to be the end of the time window where the β value first dips below
658 the line (indicated by the stars). If the β value never dips below 2, 1 year is used. For example, the
659 aftershock durations for Parkfield and Northridge are the same (>1 year).
660
- 661 **Figure 4.** Depiction of how the Coulomb stress change area is calculated. For illustration, a contour is
662 drawn around the boundary of cells with a positive Coulomb stress change of >1 MPa or more. The
663 Coulomb stress change area is given by the sum of the area of these cells.
664
- 665 **Figure 5.** Plot of the data types used for each slip inversion, where the ratios are calculated using the
666 relocated catalogs. SGM: Strong ground motion; Teleseismic: Teleseismic waveform data; Geodetic: GPS,
667 INSAR.
668
- 669 **Figure 6.** Aftershock zone area ratios for different earthquakes using different earthquake catalogs. If there
670 are multiple slip inversions for the same earthquake, the ratios are slightly offset so that they do not overlap.
671 The error bars are calculated using slip contours of 0.1 and 0.2 of the maximum slip to calculate different
672 rupture areas. (Top) NCEDC data is used to calculate the aftershock zone area for the first 3 earthquakes,
673 while SCEDC data is used for the rest of the earthquakes. (Bottom) ANSS catalog is used. The ratio for the
674 Whittier Narrows (WN) earthquake is not obtained from the ANSS catalog because the data does not yield
675 a robust estimation of the magnitude of completeness.
676
- 677 **Figure 7.** Aftershock ratios calculated from 1-day aftershock durations for both earthquake catalogs. The
678 aftershock ratios for the whole duration is plotted in the background in light grey for comparison.
679
- 680 **Figure 8.** Aftershock zone area vs. Coulomb stress change area.
681
- 682 **Figure 9.** Robust fitting (solid line) and least squares fitting (dashed line) of ratios of Coulomb stress area
683 to aftershock zone area with magnitude.
684
- 685 **Figure 10.** Illustration of how the distances from slip contour are calculated using the Parkfield, Chen Ji et
686 al slip model.
687
- 688 **Figure 11.** Histogram of aftershock distances from slip contours for all earthquakes using the relocated and
689 ANSS catalogs.
690

691 **List of Tables**

692

693

694

695

Table 1
Summary of the source properties and ratios of earthquakes.

Earthquake	Date	Location N/W	Magnitude (Mw)	Depth (km)	Slip Inversion References	Data Sources*	Reloc.	ANSS
South Napa (SN)	2014/08/24	38.22/122.31	6.10	11.0	Wei et al (2015)	SGM	1.04	0.92
			6.07	10.0	Gallovič (2016)	SGM	4.16	3.66
			5.90	8.0	Ji (2004)	SGM, GPS	1.28	2.04
Parkfield (Pf)	2004/09/28	35.82/120.37	6.00	8.3	Dreger et al (2005)	SGM, GPS	2.37	2.70
			6.06	8.3	Custodio et al (2005)	SGM	2.36	2.18
			6.98	17.6	Zeng and Anderson (2000)	SGM	5.38	4.54
Loma Prieta (LP)	1989/10/18	37.04/121.88	6.94	17.6	Wald et al (1991)	SGM, TELE	4.19	3.53
			6.96	17.6	Beroza (1991)	SGM	3.82	5.23
			6.91	17.6	Emolo and Zollo (2005)	SGM	3.40	4.69
Brawley Swarm (BS)	2012/08/26	33.02/115.54	5.45	6.4	Wei et al (2013)	SGM, GPS	0.82	2.29
El-Mayor- Cucapah (EMC)	2010/04/04	32.30/115.30	7.35	10.0	Mendoza and Hartzell (2013)	TELE	2.17	2.61
			7.29	5.5	Wei et al (2011)	TELE, SPOT, GPS, INSAR, SAR	1.79	1.74
Hector Mine (HM)	1999/10/16	34.59/116.27	7.24	6.0	Kaverina et al (2002)	SGM, GPS	1.26	1.18
			7.16	15.0	Jonsson et al (2002)	GPS, INSAR	1.49	0.98
			6.71	17.5	Zeng and Anderson (2000)	SGM	2.33	3.01
Northridge (Nr)	1994/01/17	34.21/118.54	6.80	17.5	Wald et al (1996)	SGM, TELE, GPS	1.30	1.88
			6.81	17.5	Hudnut et al (1996)	TRIL, GPS	1.38	1.67
			6.73	17.5	Hartzell et al (1996)	SGM	1.21	1.49
			7.20	7.0	Zeng and Anderson (2000)	SGM	1.18	0.88
Landers (Ld)	1992/06/28	34.20/116.43	7.22	7.0	Hernandez et al (1999)	SGM, GPS	1.80	1.26
			7.29	7.0	Cotton and Campillo (1995)	SGM	1.47	1.15
Joshua Tree (JT)	1992/04/23	34.00/116.32	6.25	12.5	Bennett et al (1995)	TRIL, GPS	2.12	1.96
Elmore Ranch (ER)	1987/11/24	33.08/115.80	6.52	10.0	Larsen et al (1992)	TRIL, GPS	4.30	2.06
Whittier Narrows (WN)	1987/10/01	34.05/118.08	5.89	14.6	Hartzell and Iida (1990)	SGM	1.61	NA
North Palm Springs (NPS)	1986/07/08	34.00/116.57	6.14	11.0	Hartzell (1989)	SGM	0.54	0.79
			6.21	11.0	Mendoza and Hartzell (1988)	TELE	1.87	2.72

696 *SGM: Strong ground motion, TELE: Telesismic data, GPS: Global Positioning System, SAR: Synthetic-
697 Aperture Radar, INSAR: Interferometric Synthetic-Aperture Radar, SPOT: Optical imaging from the
698 SPOT-5 satellite.

699

700

701

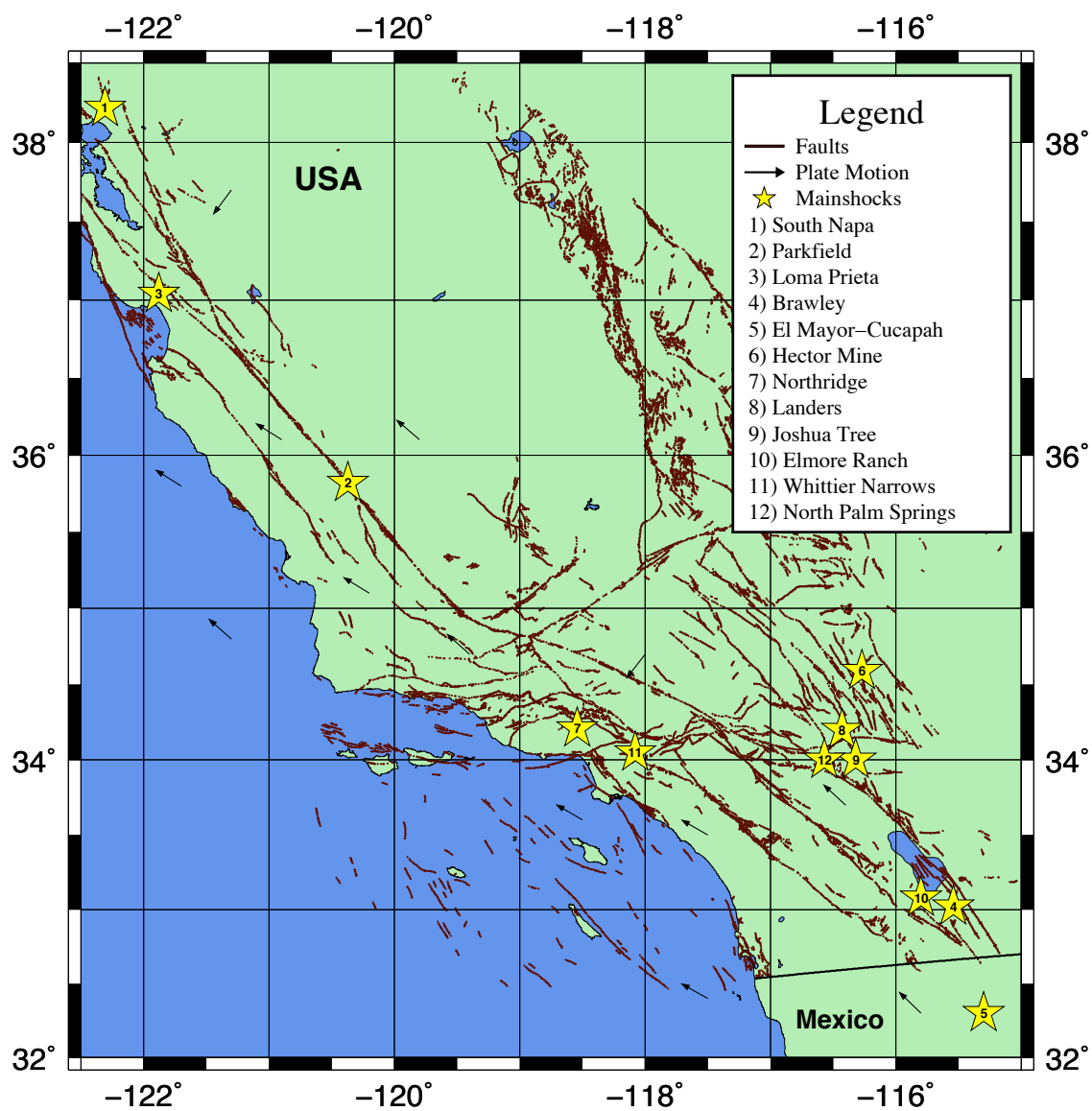
702
703
704
705

Table 2
Statistics of the ratios

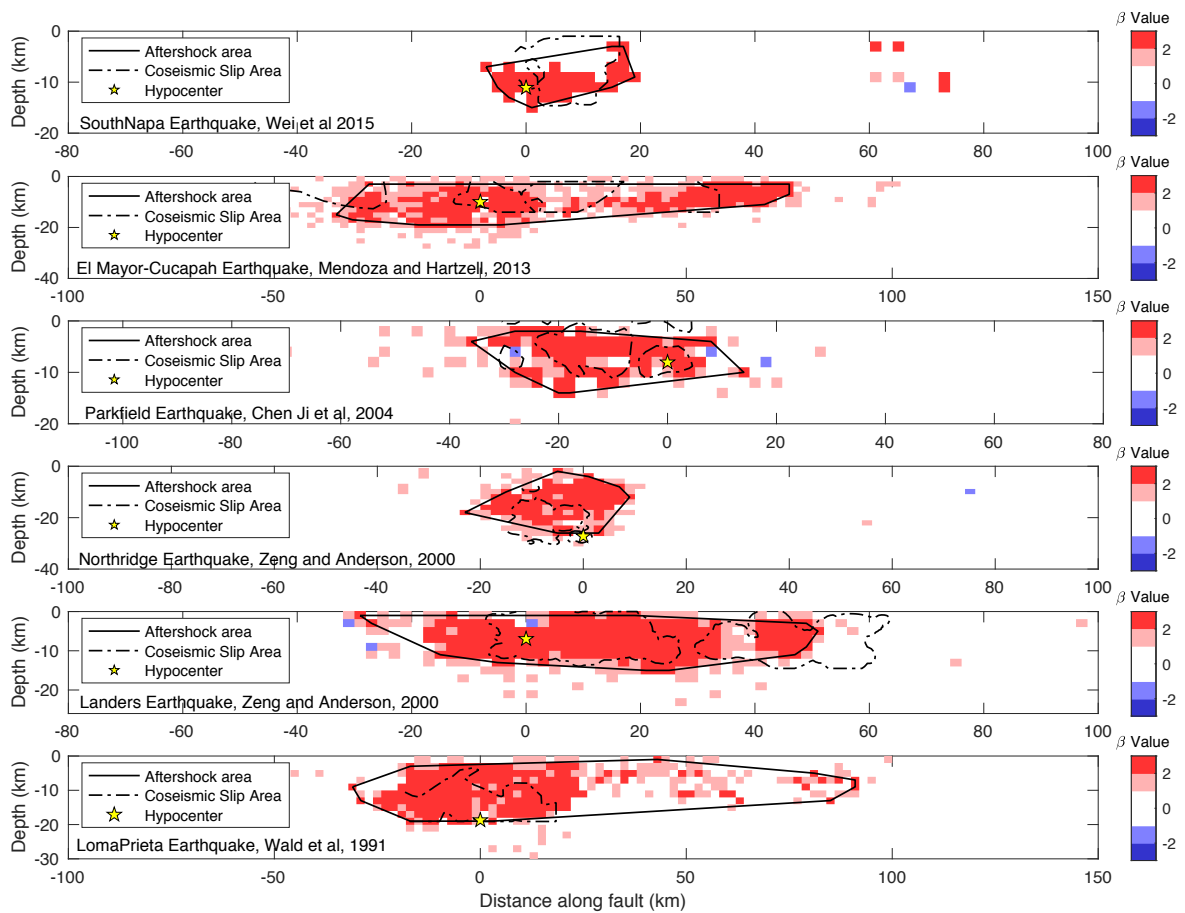
	Entire Duration		1-Day Aftershocks	
	Reloc. Catalogs	ANSS Catalog	Reloc. Catalogs	ANSS Catalog
Mean	2.18	2.16	1.83	1.70
Variance	1.58	1.90	0.84	1.07
Median	1.80	2.00	1.71	1.75
Mean Absolute Deviation	0.98	1.03	0.77	0.84

706
707
708

709
710
711
712

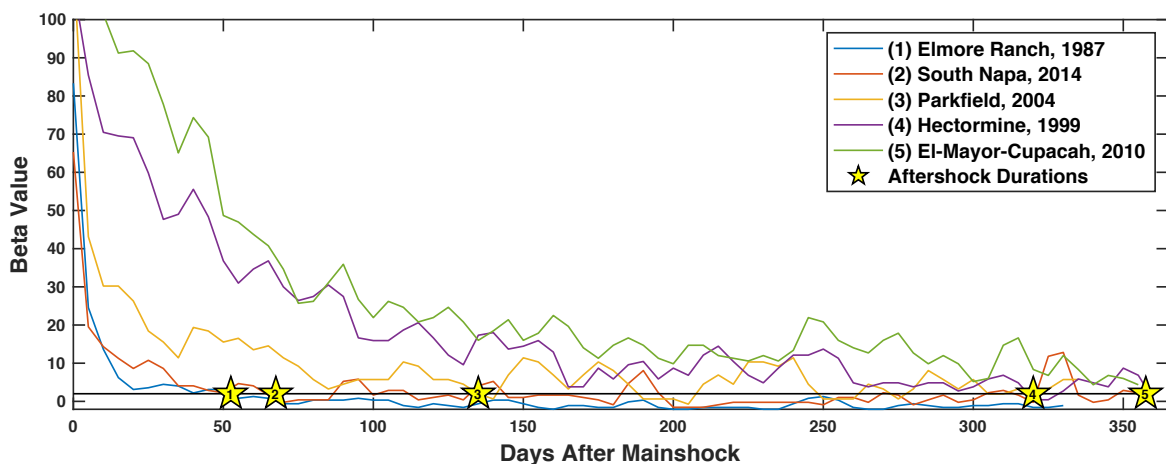


714
 715 **Figure 1.** Map of mainshock locations in this study. Known faults are specified as dark red lines, and the
 716 direction of plate motion is indicated by black arrows.



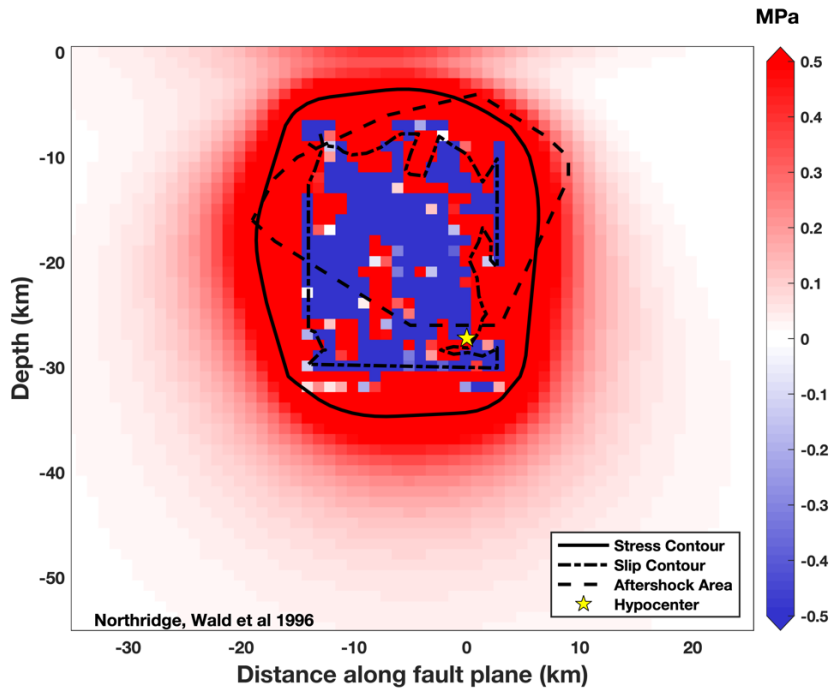
717

718 **Figure 2.** Illustration of how the aftershock zone area of each mainshock is defined using the β values. The
 719 diagrams show the fault plane view, with β values of each grid cell calculated from the aftershocks
 720 projected on to the fault plane. Aftershocks from the relocated catalogs are used for this figure.
 721

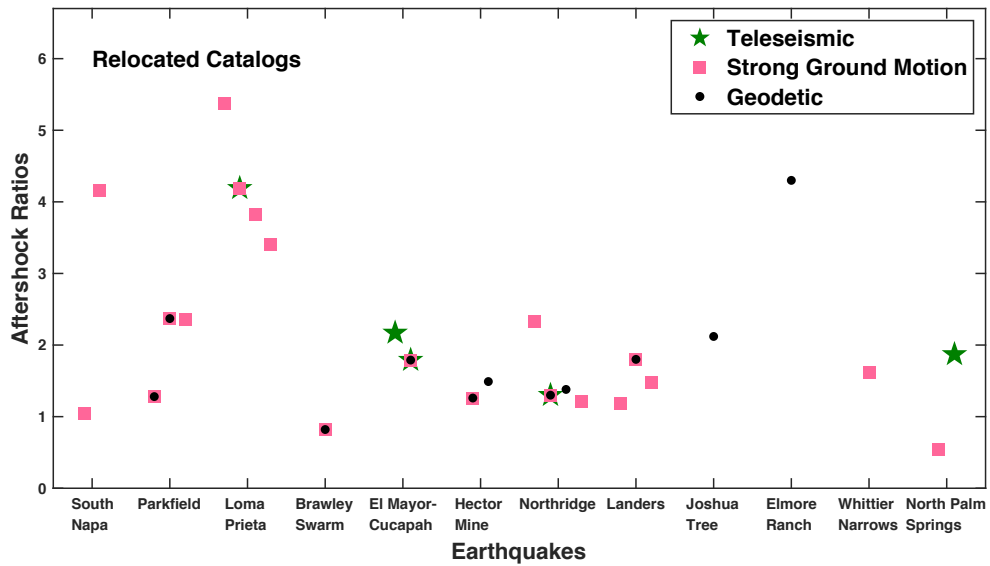


722 **Figure 3.** Illustration of how aftershock duration is calculated. The horizontal black line is at a β value of
 723 2, and the aftershock duration is taken to be the end of the time window where the β value first dips below
 724 the line (indicated by the numbered stars). If the β value never dips below 2, 1 year is used.
 725

726

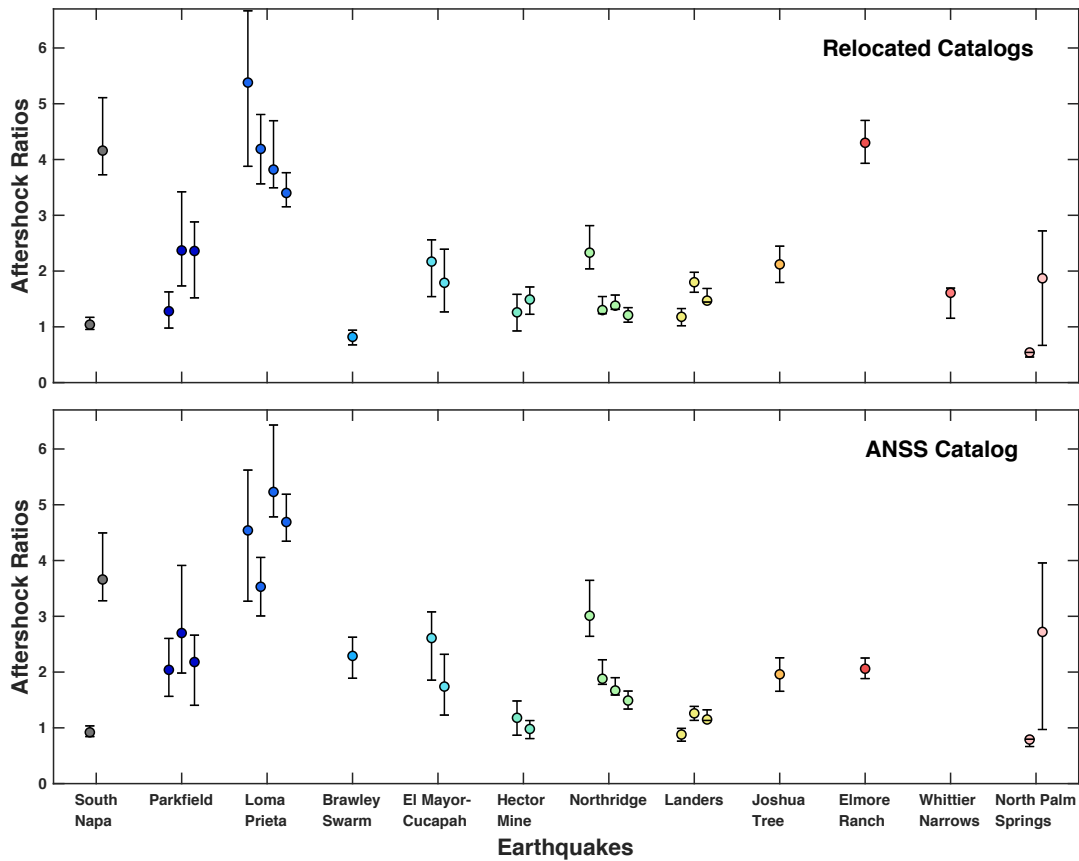


727
 728 **Figure 4.** Depiction of how the Coulomb stress change area is calculated. For illustration, a contour is
 729 drawn around the boundary of cells with a positive Coulomb stress change of >1 MPa or more. The
 730 Coulomb stress change area is given by the sum of the area of these cells.
 731

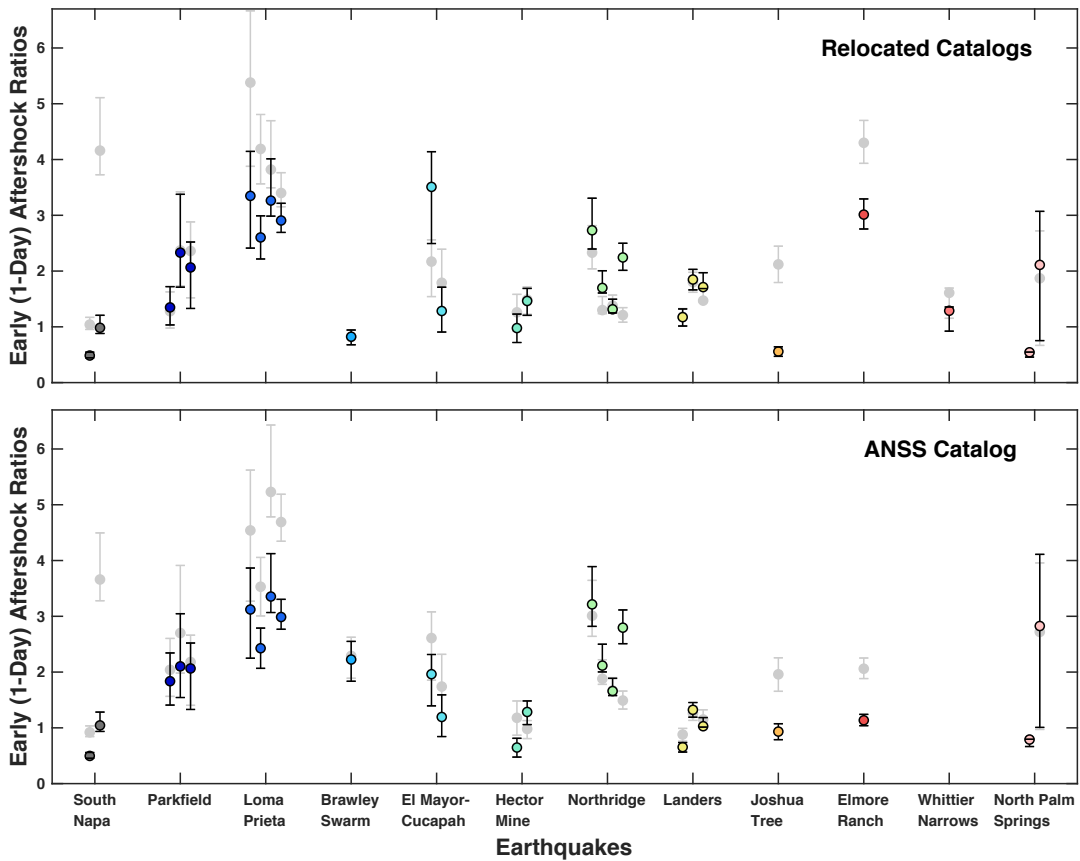


732
 733 **Figure 5.** Plot of the data types used for each slip inversion, where the ratios are calculated using the
 734 relocated catalogs. SGM: Strong ground motion; Teleseismic: Teleseismic waveform data; Geodetic: GPS,
 735 INSAR.

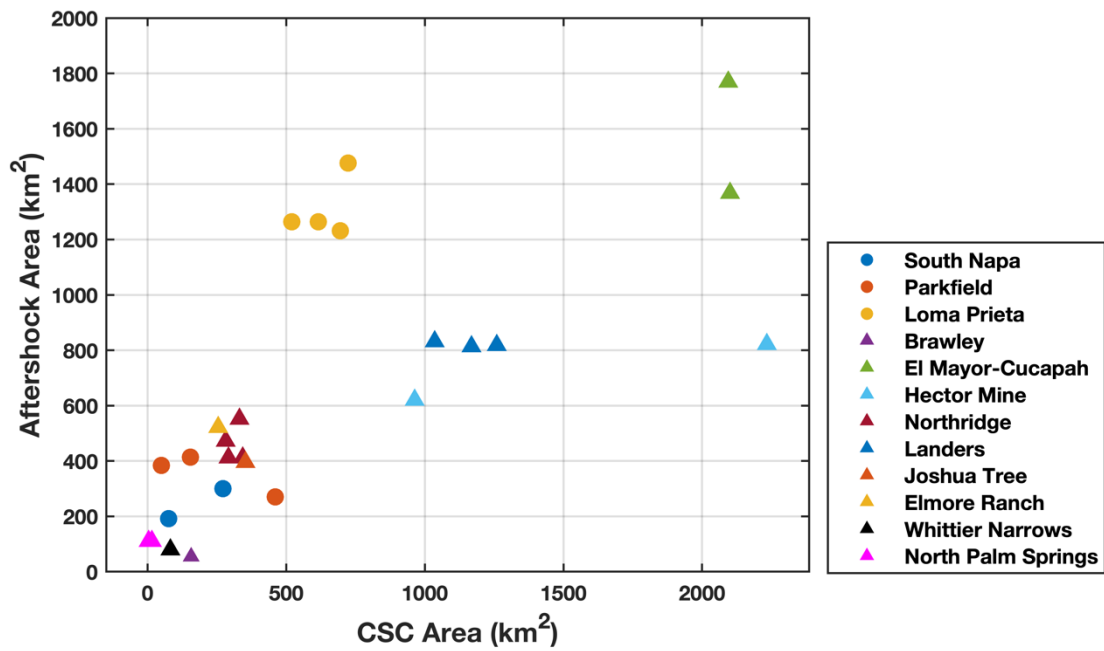
736



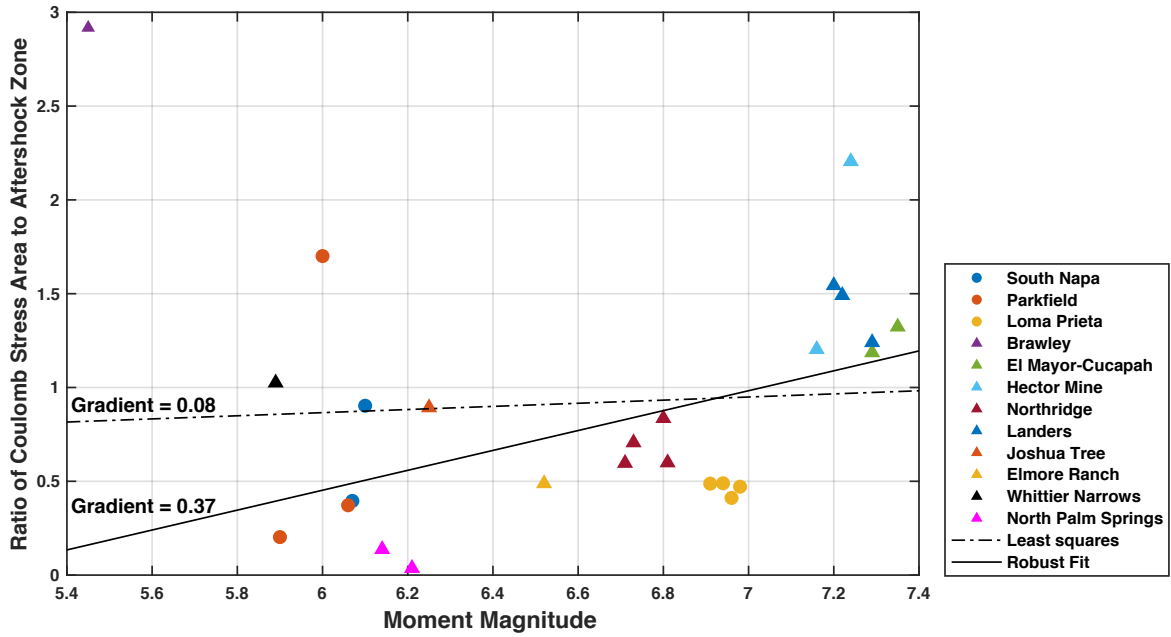
737
 738 **Figure 6.** Aftershock zone area ratios for different earthquakes using different earthquake catalogs. If there
 739 are multiple slip inversions for the same earthquake, the ratios are slightly offset so that they do not overlap.
 740 The error bars are calculated using slip contours of 0.1 and 0.2 of the maximum slip to calculate different
 741 rupture areas. (Top) NCEDC data is used to calculate the aftershock zone area for the first 3 earthquakes,
 742 while SCEDC data is used for the rest of the earthquakes. (Bottom) ANSS catalog is used. The ratio for the
 743 Whittier Narrows (WN) earthquake is not obtained from the ANSS catalog because the data does not yield
 744 a robust estimation of the magnitude of completeness.
 745
 746



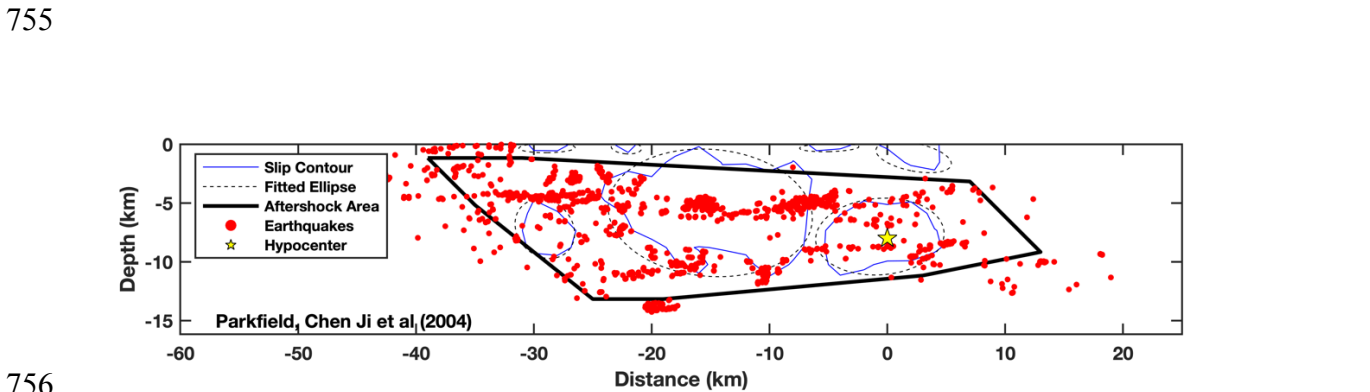
747
 748 **Figure 7.** Aftershock ratios calculated from 1-day aftershock durations for both earthquake catalogs. The
 749 aftershock ratios for the whole duration is plotted in the background in light grey for comparison.



750
 751 **Figure 8.** Aftershock zone area vs. Coulomb stress change area.

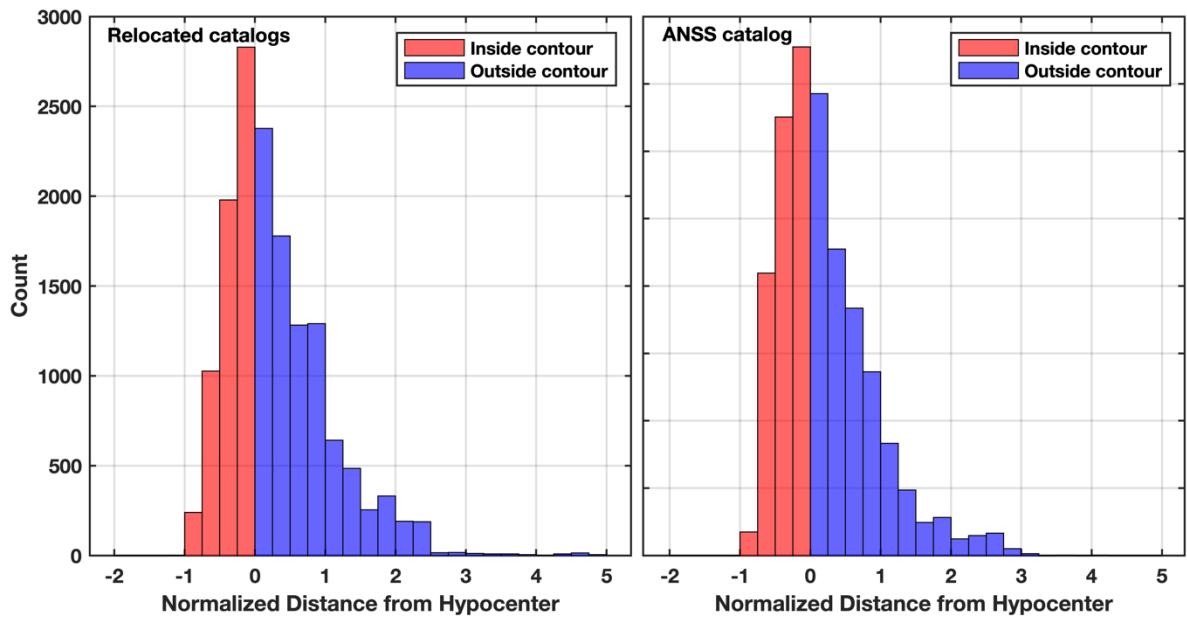


752
 753 **Figure 9.** Robust fitting (solid line) and least squares fitting (dashed line) of ratios of Coulomb stress area
 754 to aftershock zone area with magnitude



756
 757 **Figure 10.** Illustration of how the distances from slip contour are calculated using the Parkfield, Chen Ji et
 758 al slip model.

759



760
 761 **Figure 11.** Histogram of aftershock distances from slip contours for all earthquakes using the relocated and
 762 ANSS catalogs.

763